



Deformation mechanisms in meta-stable and nitrogen-stabilized austenitic stainless steel during severe surface deformation

Wang, Bo; Hong, Chuanshi; Winther, Grethe; Christiansen, Thomas L.; Somers, Marcel A. J.

Published in:
Acta Materialia

Link to article, DOI:
[10.1016/j.mtla.2020.100751](https://doi.org/10.1016/j.mtla.2020.100751)

Publication date:
2020

Document Version
Publisher's PDF, also known as Version of record

[Link back to DTU Orbit](#)

Citation (APA):
Wang, B., Hong, C., Winther, G., Christiansen, T. L., & Somers, M. A. J. (2020). Deformation mechanisms in meta-stable and nitrogen-stabilized austenitic stainless steel during severe surface deformation. *Acta Materialia*, 12, Article 100751. <https://doi.org/10.1016/j.mtla.2020.100751>

General rights

Copyright and moral rights for the publications made accessible in the public portal are retained by the authors and/or other copyright owners and it is a condition of accessing publications that users recognise and abide by the legal requirements associated with these rights.

- Users may download and print one copy of any publication from the public portal for the purpose of private study or research.
- You may not further distribute the material or use it for any profit-making activity or commercial gain
- You may freely distribute the URL identifying the publication in the public portal

If you believe that this document breaches copyright please contact us providing details, and we will remove access to the work immediately and investigate your claim.



Full Length Article

Deformation mechanisms in meta-stable and nitrogen-stabilized austenitic stainless steel during severe surface deformation

Bo Wang*, Chuanshi Hong, Grethe Winther, Thomas L. Christiansen, Marcel A.J. Somers

Department of Mechanical Engineering, Technical University of Denmark, DK-2800 Kongens Lyngby, Denmark



ARTICLE INFO

Keywords:

AISI 304L stainless steel
High-temperature solution nitriding
Surface roller burnishing
Deformation-induced martensitic transformation
Austenitic nanocrystallites

ABSTRACT

AISI 304L stainless steel in austenitized and in solution nitrided condition was severely mechanically deformed by surface roller burnishing. High-temperature solution nitriding was applied to achieve a nitrogen-concentration depth profile, leading to a depth-gradient in the austenite stability. X-ray diffraction, electron microscopy and hardness indentation were applied for characterization of the graded microstructures obtained by combining a composition profile and a deformation profile. While severe plastic surface straining of an austenitized specimen leads to a deformation-induced transformation of austenite into martensite, the solution nitrided specimen remains austenitic upon deformation, even in the region where nanocrystallization occurs. The deformation mechanisms operable in the nitrogen-stabilized austenitic stainless steel, i.e. twinning or dislocation glide, depend on the combination of applied plastic strain/strain rate, and the nitrogen-concentration dependent stacking fault energy.

1. Introduction

Metastable austenitic stainless steels are materials of high interest for a plethora of engineering applications due to their intrinsically high corrosion resistance and good formability [1]. One of the most efficient ways to achieve reasonable strength and fatigue resistance in these materials is severe plastic surface deformation (SPSD). Conventionally, SPSPD, such as ultrasonic shot peening, deep rolling and surface mechanical attrition treatment (SMAT), leads to significant microstructural changes associated with grain refinement to submicron-/nano-meter dimensions, formation of micron-scale defects and deformation-induced martensitic transformation [2–5]. Despite a positive contribution to strength, the presence of deformation-induced martensite (i) negatively influences the resistance against aqueous corrosion; (ii) increases the susceptibility to hydrogen embrittlement; (iii) results in a reduction in the ductility and (iv) is particularly harmful during low-temperature surface nitriding [6–11]. Therefore, the prevention of deformation-induced martensite upon SPSPD is necessary for metastable austenitic stainless steels subjected to forming applications.

Nitrogen is a potent austenite stabilizer and offers beneficial effects for austenitic stainless steels, involving enhanced yield strength without significant reduction in ductility, improved electrochemical properties and a reduction of the nickel content as austenite stabilizer [12–14]. Nitrogen can be introduced to stainless steels in the liquid state to manufacture a so-called high nitrogen steel or in the solid state at

elevated temperature by thermochemical treatment in a nitrogen-containing gaseous atmosphere. Both procedures are viable means to stabilize austenite from transforming into martensite on deformation and both are applied in industrial practice. Dissolution of nitrogen into the liquid phase is associated with a relatively low maximum nitrogen solubility and requires high pressure electroslag remelting [13–15]. Dissolution in the solid state can be achieved by high-temperature solution nitriding (HTSN), and is limited in the depth range [16,17]. The achievable case depth is several hundred microns (up to a few mm's) deep and depends on the process conditions. The nitrogen content at the surface reflects equilibrium between gas and solid and depends on the alloy composition, the applied temperature and the (total or partial) N_2 pressure in the gas [11]. In previous research activities, HTSN was utilized for suppressing the martensitic transformation during subsequent cold drawing [10] or rolling [18,19] of type AISI 304 steel. These investigations confirmed that effective stabilization of austenite can be achieved by introducing nitrogen in solid solution. This suggests the possibility of severe deformation of austenite that has been stabilized by prior HTSN, and thereby potentially the development of a nano-crystalline surface layer in austenite.

The effect of nitrogen on deformation mechanisms in austenite is likely to be associated with a modification of the stacking fault energy (SFE), which plays a key role in the operable deformation mechanism in austenitic stainless steels - phase transformation, twinning, or dislocation glide by slip and the associated strain hardening behavior

* Corresponding author.

E-mail address: bwang@mek.dtu.dk (B. Wang).

[20–22]. The dependence of SFE on the nitrogen content is not accurately known, as conflicting values can be found in the scientific literature [10,20,21,23]. It is anticipated that a variation of nitrogen content with depth, as obtained after HTSN, is associated with a depth-distribution of SFE in the solution nitrided case. This, coupled with a depth-gradient in the degree of deformation and the strain rate as induced by SPSSD, provides a means to track the microstructure characteristics at different levels of plastic strain, strain rate, and SFE.

In the present work, a commercial AISI 304L stainless steel is HTSN treated and subsequently severely deformed by surface roller burnishing (SRB). The objectives of the present study, are (i) to establish a nitrogen-concentration depth profile and associated gradient in the austenite stability prior to SRB, (ii) to interpret the austenite stabilization and microstructure evolution at different levels of strain, strain rate, and SFE, and (iii) to develop a novel approach to obtain a graded nanostructured/ultrafine surface layer without martensite formation.

2. Experimental procedure

The starting material AISI 304L stainless steel was provided as plates with size of 70 mm × 30 mm × 3 mm in annealed condition. The chemical composition of the alloy is (in wt %): 0.023 C, 18.35 Cr, 8.51 Ni, 0.41 Si, 0.83 Mn, 0.03 P, 0.004 S and balance Fe; the SFE for an alloy with this composition is ~ 18 mJ/m² [20].

The specimens were solution nitrided at 1150 °C (1423 K) for 2 h in 0.5 bar N₂ (total pressure). As a reference one as-received plate was subjected to a solution heat treatment (SHT), i.e. an austenitization, at the same temperature and for the same time in argon at atmospheric pressure. Both treatments were terminated by high-pressure gas quenching to avoid austenite decomposition and/or the formation of nitride precipitates during cooling. Subsequently, the surfaces of the SHT and HTSN specimens were severely plastically deformed through SRB based on a pin-on-disk configuration similar to that described in Ref. [24]. During SRB, the roller was pressed against the surface of a steel plate mounted on a turning lathe, while the steel plate rotated at a speed of 300 rpm. The roller was made of high speed steel and has a hardness of HV 720–772. The roller is 8 mm wide and has a radius of curvature of 6 mm. The roller rolled onto the surface of the plate and was simultaneously traveled back and forth at 0.038 mm/revolution in the radial direction of the rotating plate. Thus, a circular region of 30 mm in diameter was processed on each specimen. In order to obtain different degrees of deformation, two feed depths, i.e. the maximum depth of the roller into the plate, were applied: 300 μm and 500 μm. A surface roughness of S_a=0.3 μm was achieved under the applied SRB feed depth range. Metalworking water soluble coolant Quaker cool 7350 BFF was applied for cooling and lubricating during the SRB process.

Glow discharge optical emission spectroscopy (GD-OES by Horiba Jobin Yvon GD profiler 2) was applied to determine the nitrogen concentration profile after HTSN; depth-profiling was achieved in a plasma at 1000 Pa and 40 W. Since the depth range of nitrogen is beyond the depth range of accurate GD-OES depth profiling, the nitrogen concentration profile was measured using spot measurements at multiple locations, starting from different depths on the specimen as realized by successively removing thin layers by gentle polishing. Quantification of the nitrogen concentration profile was achieved using reference materials, including a nitrogen-free AISI 304L stainless steel and a JK 49 steel with a nitrogen content of 2 wt %. Thermodynamic equilibrium calculations related to solution nitriding of the alloys were performed using Thermo-Calc 2017b with the TCFE Steels/Fe-Alloys v6.2 database.

A Bruker D8 AXS X-ray diffractometer with Cr K α radiation was used to identify the crystalline phases in surface or subsurface of the treated specimens. To study the structures along the depth direction using XRD investigation, the specimen was examined at different depths by successively electropolishing off thin layers of 19–30 μm. The cross-sections of the specimens were mechanically polished and etched at room temperature with Kalling's reagent for metallographic investigation. Reflected

light microscopy was carried out on the cross-sections with a Zeiss Jena Neophot 30 microscope to either observe the nitrided layer or differentiate the morphological features of the deformed microstructure treated at different feed depths. The microstructural evolution along sections perpendicular to the treated surface of the SRB specimens was further investigated using a combination of electron channeling contrast imaging (ECCI) and electron backscatter diffraction (EBSD) on a Zeiss Supra 35 scanning electron microscope (SEM). ECCI was performed at 15 kV acceleration voltage and a working distance of 6–7 mm, depending on the specimen shape. For the EBSD procedure, the cross-section of the specimen was electropolished in a "Struers Electrolyte A2" solution at 25 V for ~30 s in a LectroPol-5 electrolytic polishing machine. EBSD analysis was performed on a selection of regions with a step size of 30 nm using an accelerating voltage of 20 kV. A thin foil with size of 8 μm × 9 μm was extracted perpendicularly to the feed direction in the outermost surface region by a focused ion beam (FIB) facility (Tescan Lyra 3 GMU) to achieve a reliable observation of the ultrafine structure. The specimen thus prepared was welded onto a platinum clamp and examined in an FEI Tecnai T20 Transmission Electron Microscope (TEM), operated at an accelerating voltage of 120 kV. The hardness distribution in the nitrided/deformed surface layers was measured using a Future-Tech FM-700 hardness tester applying a load of 25 g at a dwelling time of 10 s at various depths. Presented hardness values are the average of 5 indentations.

3. Results

3.1. Solution nitriding treatment

The effect of solution nitriding was verified by comparison of the HTSNed microstructure and the nitrogen concentration profile with those in as-annealed 304L specimen by means of thermodynamic calculation and experimental evaluation. An isopleth showing the evolution of phase stability with nitrogen content, displays the γ -phase field in the temperature range 800 °C to 1350 °C in Fig. 1(a). Iso activity lines as referred to by the given N₂ pressures are superimposed on the isopleth, so the equilibrium nitrogen content is given as a function of temperature and N₂ pressure.¹ HTSN conditions of 1150 °C and 0.5 bar were selected such that the γ -phase is stable for the entire composition range from 0.42 wt % at the surface, in equilibrium with the N₂ gas, to the nitrogen-free core. No chromium nitrides are expected to develop during nitrogen dissolution. The experimental nitrogen concentration profile along the diffusion direction is shown in Fig. 1b. After 2 hours of HTSN at 1150 °C, the absorbed nitrogen atoms have diffused to a depth of ~ 450 μm and the nitrogen content averaged over the first 2 μm is 0.40 wt %, in good agreement with the nitrogen content predicted by assuming thermodynamic equilibrium at the surface (Fig. 1a).

The grain size on the right-hand side of the micrograph in Fig. 1d reflects the effect of temperature on grain size, while some of the grains in the nitrogen-containing region to the left are appreciably larger. Evidently, substantial grain growth (from ~ 21 to ~ 87 μm) occurred along with the dissolution of nitrogen in the solid state at 1150 °C (cf. Fig. 1c and d). A cross-sectional micrograph of the solution nitrided specimen (Fig. 1d) shows no indications of precipitate formation at grain boundaries or in the grain interior. As long as the nitrides are avoided the nitrogen uptake through HTSN is beneficial for the electrochemical properties [25], which also leads to slower etching rates close to the surface compared with that in the core; hence, the faint microstructural details in the surface-adjacent zone.

¹ Strictly speaking this is the partial pressure of N₂ at 1 bar total pressure. However, since the total pressure has a negligible effect on the position of the phase boundaries in Fig. 1a for the pressure range considered (up to 1 bar), total and partial pressure are interchangeable.

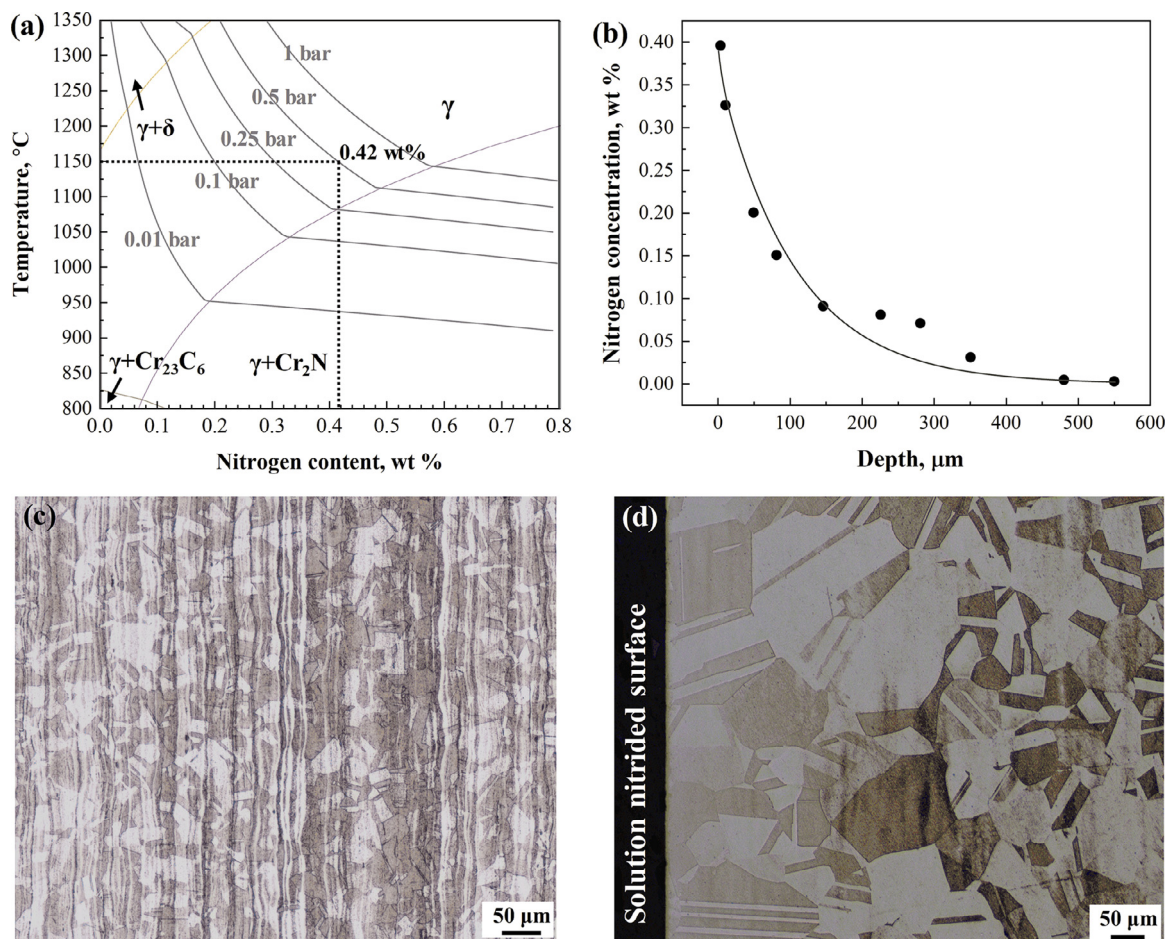


Fig. 1. (a) Calculated Fe-N phase diagram with N_2 isobars showing the phase stability of austenite and interface equilibrium conditions. (b) Experimental nitrogen concentration distribution as determined with GD-OES. Light-optical microstructures of the as-annealed specimen (c) before and (d) after solution nitriding.

3.2. Phase stability of the SRB surface layer

X-ray diffractograms from the surfaces of the SHT and HTSN specimens before and after surface roller burnishing are given in Fig. 2. The more intense 220 austenite reflection in for the HTSN specimen as compared to the SHT specimen is attributed to additional grain growth in nitrogen containing austenite (cf. Fig. 1d). Evidently, such grain growth promotes a slight change in texture favoring 110 oriented austenite grains. The response of the SHT and HTSN surfaces towards SRB is very different. Whilst the diffractogram of the surface zone of the SHT+SRB specimen shows mainly (b.c.c.) α' -martensite after SRB, the HTSN+SRB specimens only show austenite. Evidently, austenite is effectively stabilized by HTSN, resulting in austenite that is fully resistant against deformation-induced martensite formation upon severe deformation. The line profiles as measured in SHT and HTSN specimens are significantly broadened after SRB, which is attributed to a reduction in the coherently diffracting domain size and/or an increase in the micro-strains [26].

To further clarify the evolution of the phase structure along with the gradients of nitrogen concentration and strain in the deformed layer, the phase composition was assessed with X-ray diffraction at different depths in the SRB treated specimens after successively removing sub-layers by electropolishing (see Fig. 3a and b). In the SHT+SRB specimen austenite as well as b.c.c. α' and h.c.p. ϵ martensite diffraction peaks are identified. The α' -martensite peaks are present up to a relatively large depth ($> 600 \mu\text{m}$) and become more intense towards the surface; ϵ -martensite is observed in the depth range 19 – 410 μm . For the HTSN specimen deformed at the same feed depth, only austenite

diffraction peaks are detected to a depth of 405 μm , while martensite does appear beyond this depth, where the nitrogen content is very low (cf. Fig. 1b). Quantitative estimation of phase fractions was carried out using the direct comparison method [27], according to ASTM standard E795 [28]. In the quantification procedure, the integrated intensity of the 200 and 220 reflections of austenite, the 220 and 211 reflections of α' -martensite, and of the 004 reflection of ϵ -martensite were considered. Fig. 3c presents the corresponding depth distributions of the martensite volume fraction on these two treated specimens. For the SHT+SRB specimen a sharp drop from 78 % to 46 % martensite occurs within the first $\sim 20 \mu\text{m}$ from the surface, followed by a gradual reduction of the martensite fraction. These findings are consistent with those presented in Refs. [29,30], where the amount of martensite was found to increase with the degree of deformation and a reduction of the grain size of AISI 304 stainless steel during cold working at room temperature. For the HTSN+SRB specimen, beyond 405 μm depth, the small amount of martensite detected ($< 2\%$) is comparable to the content determined in the SHT+SRB specimen at this depth (Fig. 3c). The significant difference in the volume fraction of deformation-induced martensite between the SHT+SRB and HTSN+SRB specimens indicates that for the present conditions, the combination of nitrogen content and degree of deformation is sufficient to suppress martensite formation up to a depth of $\sim 400 \mu\text{m}$. The in-depth volume fraction of martensite in the SHT+SRB specimen in Fig. 3d, shows a considerable amount of ϵ -martensite with respect to α' -martensite, especially in a range of medium degree of deformation.

For a higher feed depth of 500 μm , X-ray diffractograms at different depths for the HTSN+SRB specimen contain tiny diffraction peaks of ϵ -martensite at certain depths (Fig. 3b). Evidently, austenite is not

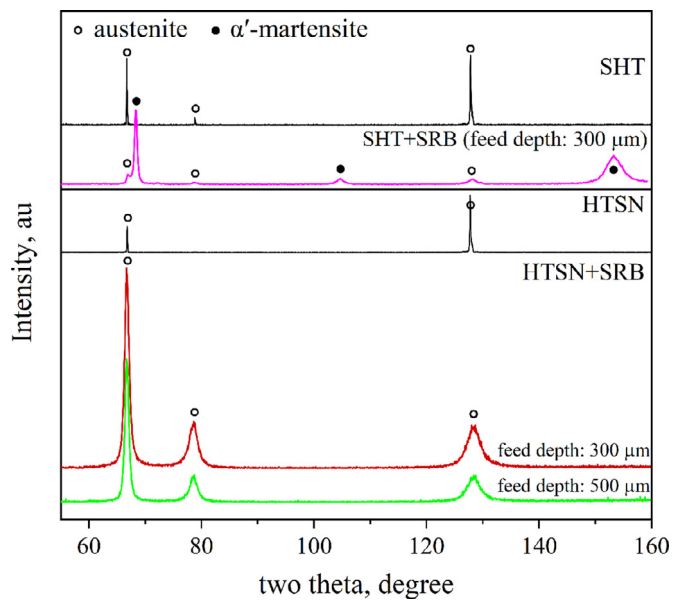


Fig. 2. X-ray diffractograms showing the phases present in the surface-adjacent zone of the solution treated/nitrided specimens before and after SRB.

sufficiently stable under this more severe deformation condition. These results suggest that ϵ -martensite is an intermediate phase during the deformation-induced transformation $\gamma \rightarrow \epsilon \rightarrow \alpha'$ in the HTSN+SRB specimen, and indicate that there exists a critical combination of nitrogen content and degree of deformation where austenite is stable against deformation-induced martensite formation.

3.3. Microstructure characterization

3.3.1. Overall observations in the deformed zone

Cross-sectional optical micrographs of the SHT+SRB and HTSN+SRB specimens are given in Fig. 4a-c, demonstrating different features of plastic deformation and microstructure refinement, corresponding to different pre-treatment/SRB conditions. Irrespective of the pre-treatment and straining conditions, in all materials SRB produced a substantial number of thin bands. A dense outermost zone with a thickness of several tens of microns can be observed in all treated specimens, suggesting the formation of ultrafine/nano-crystalline grains (see below). In good accordance with other severely surface deformed austenitic stainless steels [31–34], the plastic deformation and strain induced by SRB depend on the depth below the surface. The surface has experienced the highest plastic strain, consisting of compression, as imposed by the feed, and shear, through frictional contact with the roller. Plastic strain gradually decreases with depth and the shear component vanishes, as suggested by absence of grain boundaries that bend towards the forward roller direction. In the following the deformation response of the three treated specimens is described in separate sections.

For the SHT specimen, SRB with a feed depth of 300 μm has induced a deformed zone (below the dense surface zone) that consists of multiple thin straight bands the density of which increases towards the surface (Fig. 4a). Abundant band intersections develop in the upper part of the deformed zone, while groups of parallel bands and individual bands are visible deeper in the deformed zone.

Under the same SRB conditions, relatively few bands and hardly any band intersections are observed in the surface-adjacent region of the HTSN specimen (Fig. 4b), where a relatively high nitrogen content is present. More pronounced formation of thin bands is observed deeper ($\sim 430 \mu\text{m}$) in the deformed zone, where the nitrogen content is low, and appears to extend slightly deeper than for the SHT+SRB

specimen (Fig. 4d). The thickness of the deformed zones reflects the transferability of the plastic deformation, which depends on the dissipation of the mechanical work exerted on the specimen during SRB. Based on the processing characteristic of SRB, i.e. “repetitive mechanical loading”, the deformed microstructure developed at an earlier stage would always participate in the energy dissipation during the later deformation. The deeper deformed zone exists in HTSN+SRB specimen reveals that deformation-induced twin/dislocation possesses a higher transferability of plastic deformation than for martensite. This may be attributed to the relatively high hardness of martensite (see below the hardness results in Fig. 8), which limits the transfer of plastic deformation to deeper regions. Similar deformation morphologies are identified for a feed depth of 500 μm ; the thicknesses of the dense surface-adjacent zone and the entire deformed zone are larger than for a 300 μm feed depth (Fig. 4c and d).

It is noted that the microstructure in the surface-adjacent region of the deformed SHT specimen appears dark after etching for ~ 10 s, while the deformed surface layer on the HTSN-300 specimen remains bright, even for a relatively long etching time of 24 s (the HTSN-500 specimen is slightly electrochemically attacked in this region). This difference in electrochemical response is explained from the largely martensitic surface zone for the SHT+SRB and the nitrogen-containing austenitic surface zone for the HTSN+SRB specimens.

3.3.2. Deformed microstructure on SHT+SRB specimen

The microstructure evolution along the deformation direction in the SHT+SRB specimen is revealed by ECCI (Fig. 5a). Similar to that given in Fig. 4a, the thin bands are present in different configurations depending on depth: close to the surface, bands of a few micrometers thick are intersected abundantly, while deeper in the zone sets of parallel bands occur within the grains. The microstructure in the ultrafine surface zone as observed with light-optical microscopy (Fig. 4a) is not shown, because this part was largely dissolved during electropolishing of the cross section, consistent with its dark appearance in Fig. 4a.

A combination of ECCI and EBSD was used in three selected regions, corresponding to different depths in the deformed zone. In region I, the thin bands have a width of 1–2 μm and consist of a mixture of ϵ -martensite and α' -martensite. In particular, along a single ϵ lath there is a high density of α' -martensite, some of which are wider than the ϵ laths. These observations suggest that α' -martensite has nucleated inside the ϵ laths and thereafter has grown into the austenite matrix. Similar structures were observed in Refs. [35–37], where the growth of α' -martensite was reported to be confined by several adjacent bands. At a depth of $\sim 270 \mu\text{m}$ (region II) both individual bands and groups of bands are present. Both α' - and ϵ -martensite form in the individual bands and are separated from the neighboring phases by a sharp boundary, leading to serrated shape distribution, whereas exclusively α' -martensite is observed in the groups of bands (Fig. 5e-g). It is most likely that this α' -martensite results from a direct $\gamma \rightarrow \alpha'$ transformation without ϵ -martensite as a pre-cursor for α' -martensite, which has also been observed previously [38, 39]. At a depth of $\sim 450 \mu\text{m}$ (region III), where a relatively low degree of deformation was applied, a small number of intersected bands is found. At the intersections small units of α' -martensite have developed while the bands themselves consist of ϵ -martensite (Fig. 5h-j). The development of α' -martensite at band intersections is consistent with the commonly accepted nucleation theory stating that the intersections of ϵ -martensite or microscopic shear bands including faults and twins, are preferred nucleation sites for α' -martensite [30,40,41].

In concert with Fig. 3d, the applied plastic deformation gradient in strain/strain rate resulted in fluctuating fractions of martensite (both α' - and ϵ -martensite) with depth in the SHT+SRB specimen, without playing a significant role in altering the deformation mechanism (Fig. 5).

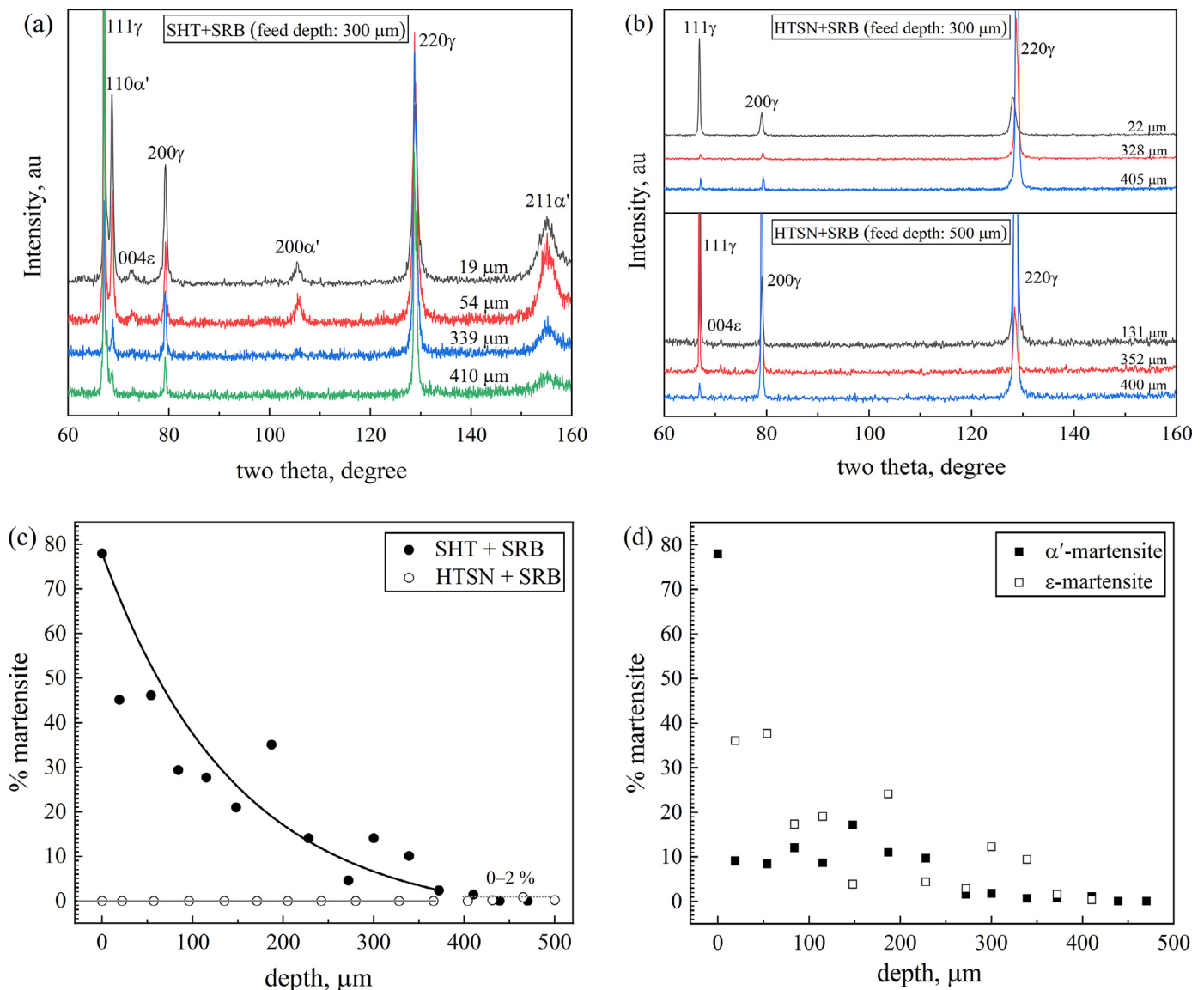


Fig. 3. Typical X-ray diffractograms obtained at different depths in (a) the SHT specimen SRBed at 300 μm feed depth, and (b) HTSN specimens SRBed at 300 μm and 500 μm feed depths. In-depth volume fraction of (c) total martensite in the two types of specimens and (d) α'-martensite and ε-martensite in the SHT+SRB specimen.

3.3.3. Deformation microstructure in HTSN+SRB specimen

• Ultrafine zone

A TEM foil was extracted from the cross-section of the HTSN+SRB specimen to examine the microstructure in the depth range 1–10 μm below the surface (Fig. 6). The microstructure close to the outermost layer (1–3 μm from surface) is characterized by nanometer-scale grains (NGs) and a high density of dislocations. Sub-micrometer-sized grains (SGs) and lamellar sub-grain structures are present beneath the nanocrystalline zone (Fig. 6a). The dark-field TEM image shows that the lamellar sub-grain structures often appear as bundles and their width in Fig. 6b has increased to ~130 nm compared with that being several tens of nanometers near the surface in Fig. 6a. The bundles are non-uniform and irregular in shape.

Thorough examination of the SGs and lamellar sub-grain structures shows the locally existence of nano-scale twin bundles, as indicated by “f” and “c” in Fig. 6a and detailed in c–g. Both regions contain fine deformation twins of 8–39 nm in thickness as found in the bright-field images

in Fig. 6c and f, and confirmed by the selected area electron diffraction (SAED) analyses in Fig. 6d and the inset in Fig. 6f, and associated dark-field images in Fig. 6e and g. Contrast variation over a distance of hundreds of nanometers is observed along the twin/matrix lamellae both in the bright-field and dark-field images, which indicates variation in crystal orientation. This is consistent with the observed stretching of some diffraction spots in the SAED patterns. Contrast variation over a distance of tens of nanometers is also noticed within the twin/matrix lamellae, suggesting the existence of a high density of dislocations. Orientation variation and a high density of dislocations are a characteristic of deformation twins found in deformed metals, especially those deformed to large strains [33,42,43]. Additionally, discontinuous contrast was found in these nano-scale twin bundles, indicating that some twin lamellae are subdivided in blocks. Dark-field imaging and SAED in Fig. 6h confirm that the NGs have a wide range of orientations, and the nanocrystalline surface zone consists entirely of austenite with an average grain size (Feret diameter, F_h) of approximately 42 nm (Fig. 6i). The nanocrystalline austenite differs considerably from that observed in

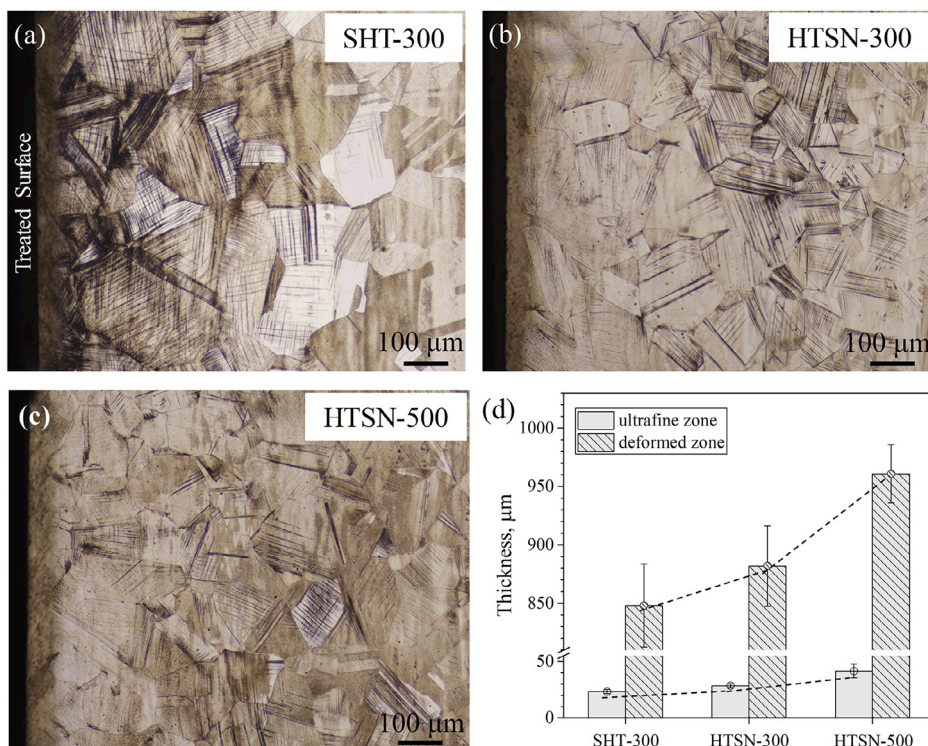


Fig. 4. Optical micrographs of deformation structures at 300 μm feed depth for (a) SHT specimen, and at (b) 300 μm and (c) 500 μm feed depth for HTSN specimens. (d) Comparison of the thickness of the ultrafine layer and the whole deformed zone induced by SRB on differently treated specimens.

the SHT+SRB specimen and other SPSD treated (metastable) austenitic stainless steels, where NGs are predominantly martensite [30–32].

• Deformed sub-surface zone

The microstructure in the deformation zone underneath the nanocrystalline zone of the HTSN specimen with 300 μm feed depth SRB is given in Fig. 7a. Interestingly, band formation is not pronounced within the depth range where solution nitriding has provided an increase in nitrogen content (up to 450 μm). A unique region at ~ 150 μm depth (marked I in Fig. 7a) shows parallel bands, as shown in Fig. 7b. The results of an EBSD investigation of the bands and surrounding areas in this region is given in Fig. 7c–e. Misorientation profiles in Fig. 7e show variations in orientation along the directions marked by arrows 1–3 in Fig. 7c and d. Misorientation profiles for arrows 1 and 3 are $\sim 60^\circ/\langle 111 \rangle$, indicating $\Sigma 3$ twin boundaries. Along the path marked by arrow 2 in the orientation map in Fig. 7c, the much smaller misorientations indicate dislocation structures formed by slip. At a depth of ~ 300 μm (region II) the focus was placed on a deformed grain, in which fence-shaped thin bands are found co-existing with an individual straight band showing a more contrasting structure (Fig. 7f). Particularly, the individual band extends through an annealing twin and exhibits a misorientation of $60^\circ/\langle 111 \rangle$ with respect to the matrix grain, confirming its twinning characteristic (Fig. 7e and 7g). In the other marked region (Fig. 7h), no typical $\Sigma 3$ -twin relationship was identified and the thin bands in the “fence” show similar features to that in a warm deformed 310 steel, for which the deformation mechanism was demonstrated to be multi-directional planar slip [44]. Austenite containing twins and dislocations and no martensite after SRB is consistent with the XRD results presented in Fig. 3b.

At 440 μm from the surface (region III in Fig. 7a), a depth commensurate with the diffusion depth of nitrogen, the formation of continuous bands is observed and becomes more pronounced with further increasing depth (Fig. 7i), similar to the deformation features in the SHT+SRB specimen (Fig. 5a). EBSD investigation in this region in Fig. 7j–n shows that the bands are mainly composed of martensite, i.e. α' -martensite forming at band groups and intersections, and complete ϵ -martensite thin plates, similar to those described in Fig. 5h–j.

3.4. Hardness

The influences of HTSN and SRB (and their combination) on the hardness-depth profile are given in Fig. 8. The dissolution of nitrogen during the HTSN treatment at 1150 $^\circ\text{C}$ for 2 h leads to a hardness of approx. 280 $\text{HV}_{0.025}$ close to the surface which decreases gradually with increasing depth until about 400 μm below surface, where the core hardness is reached. Obviously, this hardness profile is explained from solid solution strengthening by the nitrogen concentration profile.

The surface hardening effect in the HTSN+SRB specimens is enhanced with increased feed depth during SRB. For an feed depth of 500 μm the HTSN specimen reaches ~ 570 $\text{HV}_{0.025}$ close to the surface. For an feed depth of 300 μm , SRB leads to similar hardness-depth profiles for the SHT and HTSN specimens, and attains >500 $\text{HV}_{0.025}$ in the nanocrystalline region close to the surface and reaches the core hardness at a depth of approx. 1200 μm . The very high hardness values in the nanocrystalline region of SHT and HTSN specimens after SRB imply that the nano-crystalline nature, i.e. grain boundary strengthening, contributes importantly to the achieved hardness. Still the hardness close to the surface is highest in the HTSN pretreated specimen. Apart from the surface, the effect of HTSN on the hardness after SRB is mainly observed in the depth range 90–400 μm where a lower hardness is found. This is the region where no martensite has developed in the HTSN+SRB specimen, but where the SHT+SRB specimen develops martensite of about 5–30 vol.% (Fig. 3d). Evidently, beyond the nano-crystalline region, deformation-induced martensite formation contributes more effectively to a higher hardness than dislocation glide and deformation twinning in austenite.

4. Discussion

Investigation of the performance of stainless steel AISI 304L during SRB with and without prior solid-solution nitriding, shows the following important microstructural features:

- the surface-adjacent zone is nanocrystalline and consists predominantly of deformation-induced martensite for the SHT+SRB specimen and of austenite in the HTSN+SRB specimen;

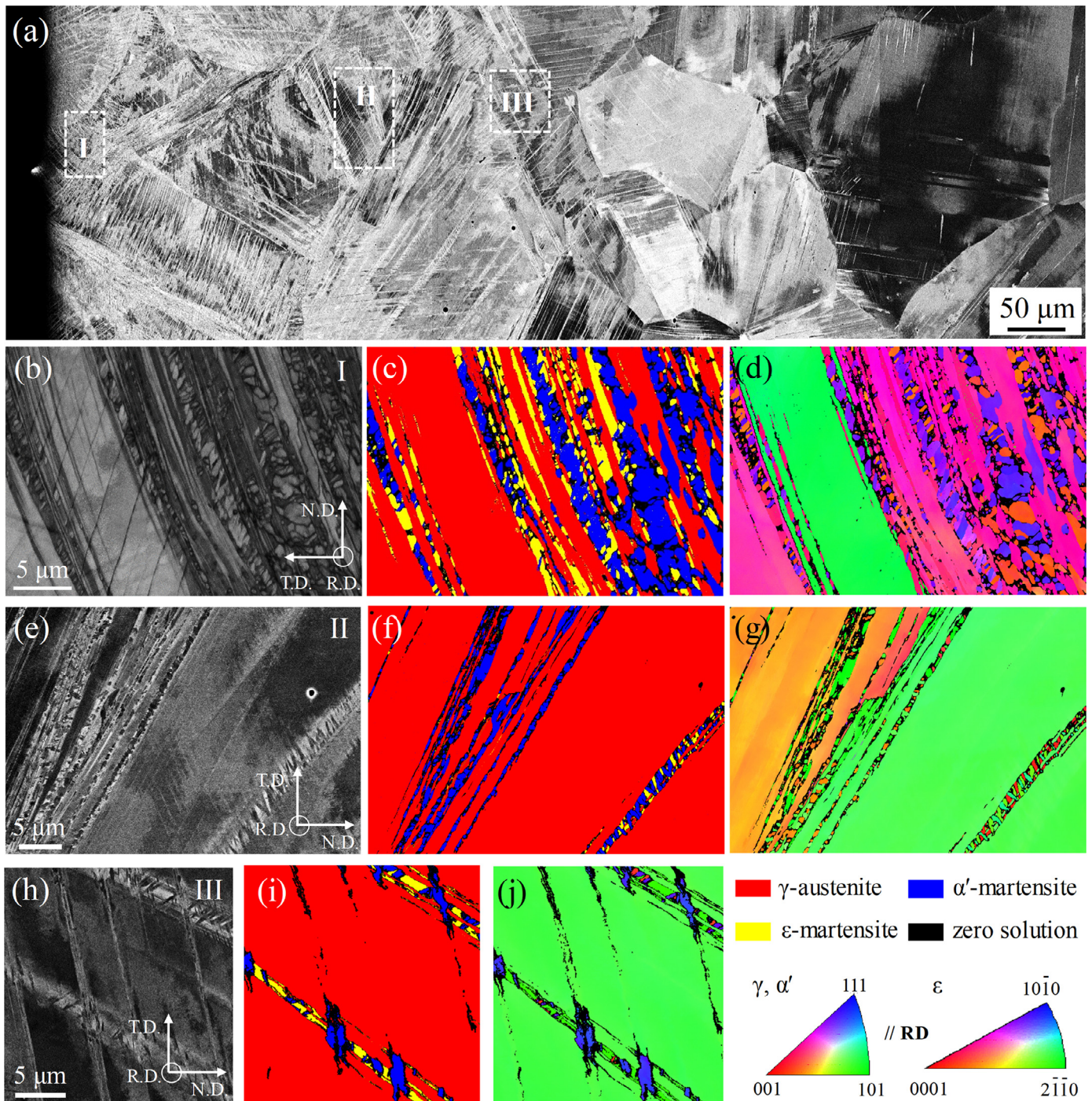


Fig. 5. Cross section of SHT+SRB specimen showing the evolution of the microstructure in: (a) ECCI image providing an overview. (b, e and h) ECCI images taken from the selected areas marked in a. (c, f, i) corresponding EBSD phase maps and (d, g, j) corresponding orientation maps.

- (ii) for the HTSN+SRB specimen the zone immediately below the nano-crystalline zone consists of SGs and lamellar sub-grain structures containing a high-density of dislocations and embedded nano-scale twin bundles;
- (iii) the deformed sub-surface zone in the HTSN+SRB specimen is fully austenitic up to a depth of $\sim 400 \mu\text{m}$, i.e. the depth range of enhanced nitrogen content after HTSN. Here slip and twinning are the only identifiable deformation mechanisms. For the SHT+SRB specimen deformation-induced formation of ϵ - and α' -martensite occurs.

4.1. Effect of nitrogen on prevailing deformation mechanisms

4.1.1. Subdivision of lamellae and formation of a nanostructure

Deformation-induced nanocrystallization on (metastable) austenitic stainless steel by SPSD has been widely reported in the literature [30–32]. Generally, formation of the nanocrystallites is considered to originate from abundant dislocation activity (forming dislocation boundaries), deformation twinning (twin-twin intersection) and martensitic phase transformation, as well as recrystallization. However, in the case of the nitrogen-stabilized specimen, deformation-induced

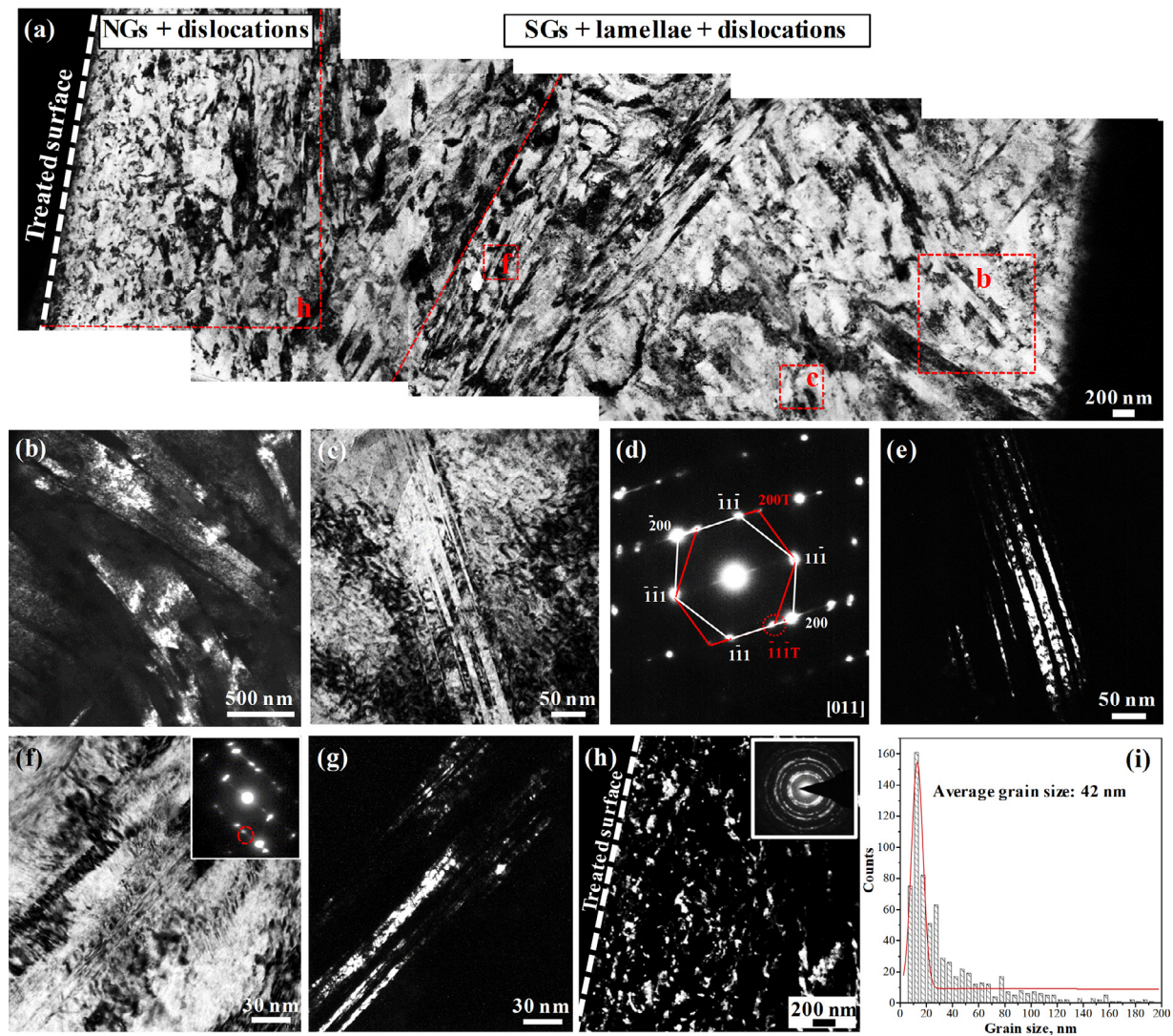


Fig. 6. (a) Cross-sectional TEM observations showing the microstructure evolution from 1–10 μm below the treated surface of HTSN+SRB specimen deformed at 300 μm feed depth. (b) Dark-field image showing typical morphology of lamellar sub-grain structures as marked in (a). (c and f) Bright-field images taken in the lamellar region as marked in (a) with higher magnification, and (d, e and g) corresponding SAED and dark-field images. (h) Dark-field image of nano-crystalline surface and (i) grain size distribution in region h.

martensite formation is suppressed and twin-twin intersection is hardly observed after SRB. On the basis of the experimental observations and analysis, it is likely that the mechanism of nanocrystallite formation in the surface of the HTSN specimens originates from the following evolution, the details of which are discussed below: (i) the formation of lamellar sub-grain structures associated with dislocation glide and twinning, (ii) the nucleation of nano-scale twin bundles embedded in the lamellae surrounded by a high density of dislocations, (iii) the subdivision of lamellae into disoriented submicron-scale grains, (iv) further breakdown of the submicron grains into randomly oriented nanograins.

Ad (i): The SRB process provides repetitive mechanical loading and appreciable shear stress onto the material's surface. As more plastic strain accumulates in the surface-adjacent region, a large quantity of dislocations is generated, giving rise to the formation of sub-grains. The sub-grains are present in a lamellar structure and consist of nano-scale twin bundles and high-density dislocations which develop continuously on straining. The twins observed in deeper zones may also play a role in promoting the formation of lamellae by providing geometrical boundaries [31,32].

Ad (ii): For increasing plastic strains, dislocation glide and twinning cannot sustain homogeneous plastic deformation and shear banding takes place. The shear bands will further split the lamellar sub-grain structure into submicron grains and the increasing strain drives the transformation from sub-grain boundaries into conventional grain boundaries with large misorientations. Analogous to SPSPed alloys, the additional strain accommodation is achieved by successive grain subdivision [2].

Ad (iii) and (iv): Close to the treated surface, the evolution of submicron-size grains into randomly oriented nanocrystallites is observed with increasing strain. Since the sizes of the nanocrystallites are approximately equal to the thickness of the nano-scale twin lamellae, the fragmentation of nano-scale twin bundles dominates the further refinement of the submicron grains. The formation mechanism of nanocrystallites via nano-twins has been investigated earlier in SPSPed alloys [33,42,43].

The deformation mechanism observed after HTSN is not limited to the applied SRB treatment, but could equally be accomplished by other SPSP processes, e.g. shot peening and SMAT. Since both HTSN and the

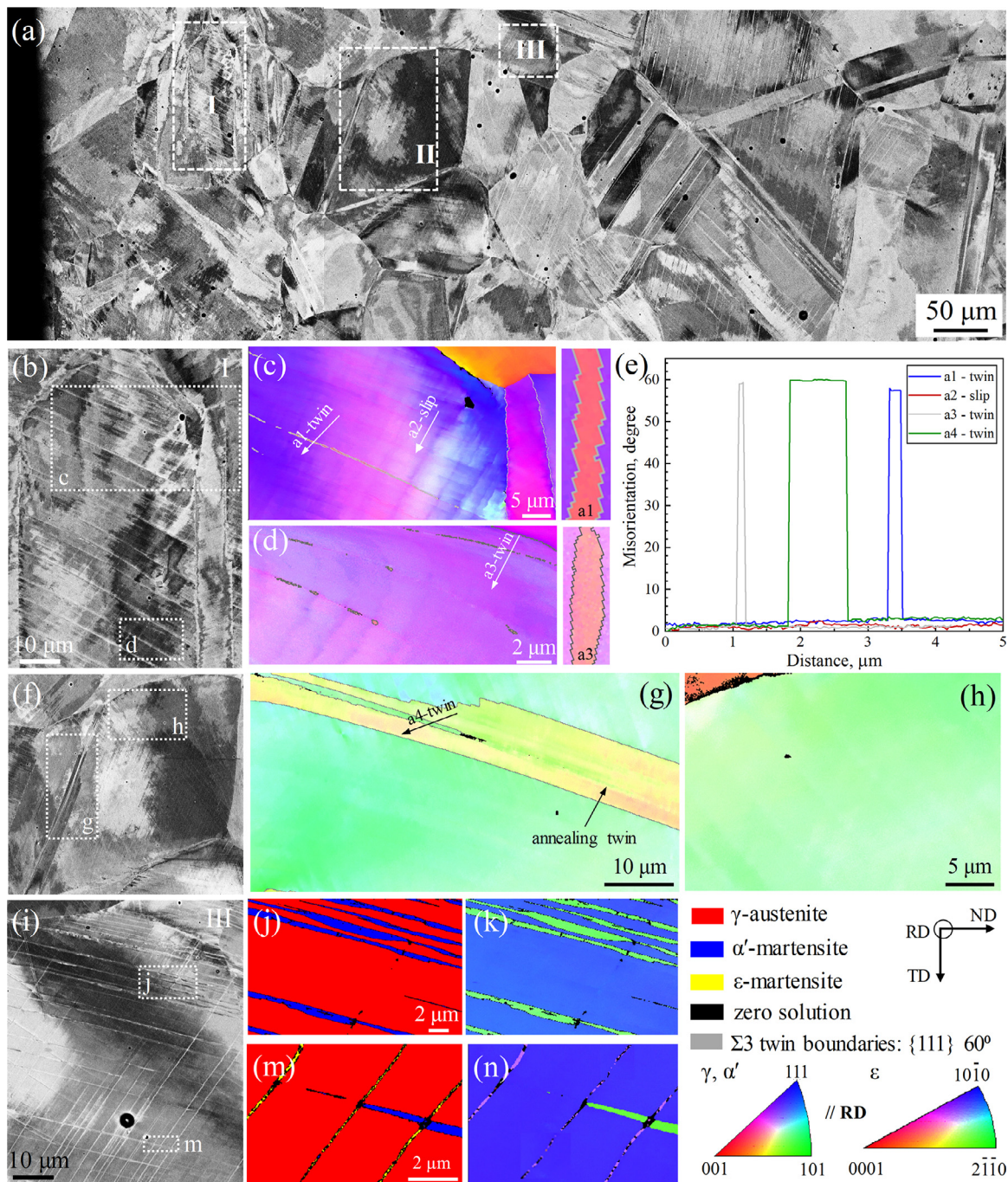


Fig. 7. Cross section of HTSN+SRB (300 μm feed depth) specimen showing the evolution of the microstructure in: (a) ECCI image as an overview. (b, f, i) ECCI images taken from the selected regions as marked in Fig. 7a and the corresponding (j, m) EBSD phase maps and (c, d, g, h, k and n) orientation maps. (e) Misorientation profiles along the directions marked by arrows 1–4 in (c, d, g).

subsequent SPSD are considered to be controllable surface engineering technologies for stainless steel, tailoring the nitrogen distribution and/or regulating the surface deformation conditions, it is reasonable to anticipate that the thickness of the austenitic nanostructured layer and the nano-twinned austenitic surface layer can be tailored.

4.1.2. Stacking fault energy (SFE)

Previous research has demonstrated that the plastic deformation behavior in face-centered cubic (FCC) metals strongly depends on the lattice structure, deformation conditions, and the SFE [2]. Despite extensive research involving experimental characterization and numerical simulations, the influence of nitrogen on SFE is so far not exactly

determined. Recently, Das [23] collected a vast amount of SFE data in different metals and alloys, which showed that nitrogen has been observed to both reduce and enhance the SFE in austenitic stainless steels. Particularly, for the range (0 ~ 0.40 wt %) of the nitrogen concentration as produced in the HTSN specimen (Fig. 1b), the value of the SFE acquired from the provided database ranges from 13 to 60 mJ/m^2 .

In the present study, the suppression of deformation-induced martensitic transformation and its replacement by twinning and dislocation glide is consistent with an increase in SFE; a monotonous dependence of SFE on nitrogen content however, was not confirmed for the present specimen. So far various experimental techniques have been applied to evaluate the SFE in FCC materials, as discussed

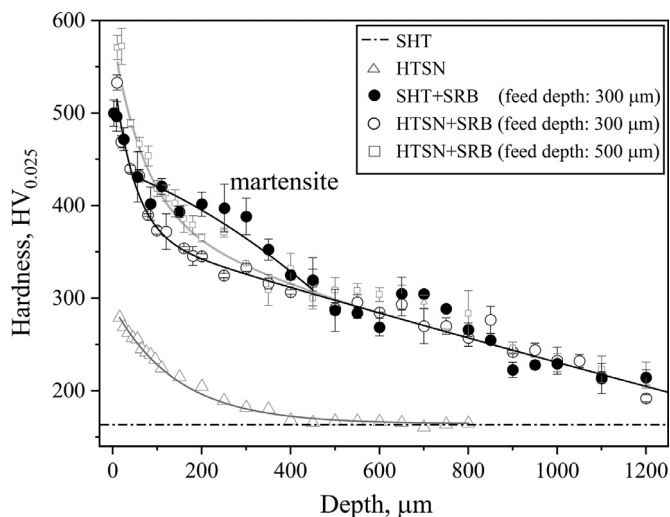


Fig. 8. Hardness depth profiles of AISI 304L in SHT and HTSN condition and subsequently SRB treated at different feed depths.

and commented in Ref. [21]. Since an alloying element as nitrogen can cause opposite changes in the SFE of alloys with different host composition [22], the relation between nitrogen content and SFE is difficult to assess unequivocally. It is worth pointing out that the nitrogen-depth profile as obtained after HTSN can be regarded as a series of thin slices of the same steel with different interstitial nitrogen contents as the only change in composition. This provides a reliable foundation and comparable composition hosts for studying the effect of nitrogen on the SFE. In the present study the gradient in nitrogen content is, however, combined with a deformation gradient, which makes the interpretation more difficult. Separation of the two effects in a series of specimens with the same steel composition and uniform nitrogen distribution adjusted by HTSN and application of (moderate) homogeneous deformation over the entire specimen thickness will enable clearer conclusions. This will be subject to future investigation.

4.1.3. Twinning vs. dislocation glide

Based on the above microstructural observations, it is observed that the two typical plastic deformation modes for FCC metals, i.e. dislocation glide and twinning, co-exist during SRB of nitrogen-stabilized 304L steel. As compared to dislocation glide, which occurs in the entire deformation zone, deformation twins were only observed in certain grains or at certain depths (Fig. 4b and 7).

It has been established that in most FCC metals, dislocations are the main carriers of plastic deformation and dislocation glide dominates at a conventional strain rate ($< 10^0 \text{ s}^{-1}$) and at ambient temperature. The critical shear stress for twinning decreases with a decrease of SFE value. Hence deformation twinning is facilitated by a lower SFE and/or favorable deformation conditions such as high strain rate and/or a low deformation temperature [45].

SRB is generally considered as low-to-medium plastic deformation since it is associated with strain rates of $10^{-3} \sim 10^{-1} \text{ s}^{-1}$ on sliding contact with the surface [46,47]. Under the given conditions of SRB in this work, the equivalent strain and strain rate are estimated to be 0.05 and $3 \times 10^0 \text{ s}^{-1}$ [48] for 300 μm feed depth, which is substantially slower than for SMAT (10^{2-4} s^{-1}). First of all, this could explain the above result that martensitic transformation in the SHT specimen is found to be $\gamma \rightarrow \epsilon \rightarrow \alpha'$, rather than $\gamma \rightarrow \gamma^{\text{twin}} \rightarrow \alpha'$ as identified in the SMATed 304 steel [32]. Secondly, it may suggest that the deformation conditions imposed by SRB provide an insufficient condition for twinning activation in AISI 304L, especially in the deeper deformed zone for moderate strain/strain rates. In addition, the onset of twinning as identified in the depth range from 130 to 170 μm for the HTSN+SRB specimen (cf.

Fig. 7b-e) indicates that the nitrogen content ($\sim 0.10 \text{ wt } \% \text{ N}$) was sufficiently enhanced to augment the SFE to a value where martensite is prevented and twinning is promoted. In the surface-adjacent zone, with approaching the surface (i.e., increasing strain and strain rate), the high density of dislocations results in an increase of the flow stress. The critical stress for twinning may be exceeded, and accordingly becomes a viable deformation mode. This explains, at least in part, the twinning behavior in the region just below the nano-crystalline zone. The TEM results (Fig. 6) confirm that appreciable plastic deformation by dislocation glide precedes deformation twinning, suggesting that dislocation glide is a precursor for twinning.

4.2. Austenite stability upon SRB

In the present study, HTSN is applied to develop a nitrogen-concentration depth profile on a metastable austenitic stainless steel plate (AISI 304L), thereby improving the austenite stability. Different from previous research activities on plastic deformation of HTSNed specimens with a nitrogen gradient/homogenous nitrogen concentration [10,18,19], or SPSP on high nitrogen steels [49,50], in the present work surface deformation by roller burnishing is performed on a nitrogen concentration profile as tailored by applying a N_2 total pressure at a selected temperature (Fig. 1a). Thus, two gradients are superimposed, a nitrogen concentration profile and a plastic strain (rate) profile.

Comparison of the microstructures in the SHT and HTSN specimens for the same deformation condition demonstrates that nitrogen dissolved by HTSN contributes importantly to stabilization of austenite against deformation-induced martensite formation (Fig. 3d). This observation would be consistent with an increase in stacking fault energy upon nitrogen dissolution, at least for the concentration range up to 0.40 wt % N in the present work. On the other hand, it is anticipated that a higher nitrogen concentration is required to further enhance the austenite stability on more severe deformation (cf. Fig. 3c). This can straightforwardly be achieved by adjusting the process parameters of the HTSN treatment, i.e. temperature, nitrogen pressure and diffusion time.

Importantly, the experiments proved the feasibility of achieving sustained austenite stability under gradient deformation conditions, in several hundreds of micrometers below the surface by modifying the nitrogen content through an HTSN treatment. Stabilizing austenite by a prior HTSN treatment allows the manufacturing of nano-crystalline austenite zone without deformation-induced martensite, hence maintaining and most likely even improving, the corrosion performance of AISI 304L [25]. On the other hand, the hardness profiles in the first 50 μm after HTSN+SRB and SHT+SRB are similar (Fig. 8), indicating that pre-hardening by nitrogen dissolution has a limited effect on the final hardness after severe surface deformation. The hardness profile for a feed-depth of 500 μm shows that the work-hardening contribution is indeed most important. Thus, for practical applications of severe surface deformation, the nitrogen content has its prime role in stabilizing austenite against strain-induced martensite formation, while plastic deformation determines the hardness profile.

5. Conclusions

AISI 304L austenitic stainless steel plates in austenitized and solution nitrided conditions were severely plastically deformed by means of surface roller burnishing. The dissolution of nitrogen by (solid) solution nitriding resulted in a case depth of $\sim 450 \mu\text{m}$ and corresponding nitrogen contents in the solid state from 0–0.40 wt. %. Such achieved depth-gradient in the nitrogen concentration led to considerable improvement in austenite stability and significant differences in microstructural features, upon the subsequent plastic deformation.

On surface roller burnishing at 300 μm feed depth, deformation-induced ϵ - and α' -martensite develops in the austenitized specimen, while a solution nitrided specimen remains fully austenitic up to a depth

of $\sim 400 \mu\text{m}$, and, in particular, in a surface-adjacent region where nanocrystallization occurred.

On both surfaces of austenitized and solution nitrided specimen, surface roller burnishing induced a deformed zone which roughly consists of an ultrafine zone at the surface and a deformed sub-surface zone. As the deformation-induced martensitic transformation mechanism is suppressed in the case of the solution nitrided specimen, the deformation response can be summarized with respect to the evolution of the deformed structure.

- Slip and twinning are the predominant deformation mechanisms in the deformed sub-surface zone based on EBSD analysis.
- Nano-crystallites in austenite are developed in the outermost surface zone. The nanocrystallization is correlated with the subdivision of the lamellar sub-grain structures containing a high-density of dislocations and embedded nano-scale twin bundles.

More severe deformation at $500 \mu\text{m}$ feed depth does induce the formation of martensite in solution nitrided specimen. The austenite stability with respect to such demanding plastic deformation can straightforwardly be achieved by tailoring the process parameters of the solution nitriding treatment, which is also realizable in commercial production.

Declaration of Competing Interest

The authors declare that they have no known competing financial interests or personal relationships that could have appeared to influence the work reported in this paper.

Acknowledgments

The research leading to these results has received funding from the European Union's Horizon 2020 research and innovation programme under the Marie Skłodowska-Curie grant agreement no. 713683 (CO-FUNDfellowsDTU) and no. 841108 (MSCA-IF).

Reference

- [1] K.H. Lo, C.H. Shek, J.K.L. Lai, Recent developments in stainless steels, *Mater. Sci. Eng. R* 65 (2009) 39–104.
- [2] K. Lu, J. Lu, Nanostructured surface layer on metallic materials induced by surface mechanical attrition treatment, *Mater. Sci. Eng. A* 375–377 (2004) 38–45.
- [3] K. Lu, N. Hansen, Structural refinement and deformation mechanisms in nanostructured metals, *Scr. Mater.* 60 (2009) 1033–1038.
- [4] I. Nikitin, I. Altenberger, Comparison of the fatigue behavior and residual stress stability of laser-shock peened and deep rolled austenitic stainless steel AISI 304 in the temperature range 25–600°C, *Mater. Sci. Eng. A* 465 (2007) 176–182.
- [5] A.Y. Chen, H.H. Ruan, J. Wang, H.L. Chan, Q. Wang, Q. Li, J. Lu, The influence of strain rate on the microstructure transition of 304 stainless steel, *Acta Mater.* 59 (2011) 3697–3709.
- [6] D.A. Vermilyea, Stress corrosion cracking of iron and nickel base alloys in sulfate solutions at 289 C, *Corros* 29 (1973) 442–450.
- [7] C.L. Briant, A.M. Ritter, The effects of deformation induced martensite on the sensitization of austenitic stainless steels, *Metall. Trans. A* 11 (1980) 2009–2017.
- [8] G. Han, J. He, S. Fukuyama, K. Yokogawa, Effect of strain-induced martensite on hydrogen environment embrittlement of sensitized austenitic stainless steels at low temperatures, *Acta Mater.* 46 (1998) 4559–4570.
- [9] T. Balusamy, T.S.N. Sankara Narayanan, K. Ravichandran, I.S. Park, M.H. Lee, Influence of surface mechanical attrition treatment (SMAT) on the corrosion behaviour of AISI 304 stainless steel, *Corros. Sci.* 74 (2013) 332–344.
- [10] F. Bottoli, G. Winther, T.L. Christiansen, K.V. Dahl, M.A.J. Somers, Low-temperature nitriding of deformed austenitic stainless steels with various nitrogen contents obtained by prior high-temperature solution nitriding, *Metall. Mater. Trans. A* 47 (2016) 4146–4159.
- [11] M.A.J. Somers, T.L. Christiansen, Thermochemical surface engineering of stainless steels with interstitials; symbiosis of science, technology and innovation, in: *Proceedings of the 26th IFHTSE Congress, Russia*, 2019.
- [12] M.O. Speidel, in: *Properties and Applications of High Nitrogen Steels*, HNS 88 Lille (France), The Institute of Metals, London, 1989, p. 92.
- [13] J.W. Simmons, Overview: high-nitrogen alloying of stainless steels, *Mater. Sci. Eng. A* 207 (1996) 159–169.
- [14] J.R. Kearns, H.E. Deverell, The use of nitrogen to improve the corrosion resistance of FeCrNiMo alloys for the chemical process industries, *Mater. Perform.* 26 (1987) 18–28.
- [15] G. Stein, I. Hucklenbroich, Manufacturing and applications of high nitrogen steels, *Mater. Manuf. Process.* 19 (2004) 7–17.
- [16] H. Berns, Manufacture and application of high nitrogen steels, *ISIJ Int.* 36 (1996) 909–914.
- [17] H. Berns, S. Siebert, High nitrogen austenitic cases in stainless steels, *ISIJ Int.* 36 (1996) 927–931.
- [18] T. Tsuchiyama, H. Takebe, K. Tsuboi, S. Takaki, Surface-layer microstructure control for metastable austenitic stainless steel to prevent hydrogen permeation, *Scr. Mater.* 62 (2010) 731–734.
- [19] T. Tsuchiyama, K. Tsuboi, S. Iwanaga, T. Masumura, A. Macadre, N. Nakada, S. Takaki, Suppression of hydrogen embrittlement by formation of a stable austenite layer in metastable austenitic stainless steel, *Scr. Mater.* 90 (2014) 14–16.
- [20] R.E. Schramm, R.P. Reed, Stacking fault energies of seven commercial austenitic stainless steels, *Metall. Trans. A* 6 (1975) 1345–1351.
- [21] T.H. Lee, E. Shin, C.S. Oh, H.Y. Ha, S.J. Kim, Correlation between stacking fault energy and deformation microstructure in high-interstitial-alloyed austenitic steels, *Acta Mater.* 58 (2010) 3173–3186.
- [22] L. Vitos, J.O. Nilsson, B. Johansson, Alloying effects on the stacking fault energy in austenitic stainless steels from first-principles theory, *Acta Mater.* 54 (2006) 3821–3826.
- [23] A. Das, Revisiting stacking fault energy of steels, *Metall. Mater. Trans. A* 47 (2016) 748–768.
- [24] C. Hong, X. Huang, N. Hansen, Gradient nanostructured surface of a Cu plate processed by incremental frictional sliding, *IOP Conf. Ser. Mater. Sci. Eng.* 89 (2015) 012026.
- [25] F. Bottoli, M.S. Jellesen, T.L. Christiansen, G. Winther, M.A.J. Somers, High temperature solution-nitriding and low-temperature nitriding of AISI 316: Effect on pitting potential and crevice corrosion performance, *Appl. Surf. Sci.* 431 (2018) 24–31.
- [26] G.K. Williamson, W.H. Hall, X-ray line broadening from filed aluminium and wolfram, *Acta Metall.* 1 (1953) 22–31.
- [27] R.D. Arnell, Determination of retained austenite in steel by X-ray diffraction, *J. Iron Steel Inst.* 206 (1968) 1035–1036.
- [28] E975-13, Standard Practice for X-ray Determination of Retained Austenite in Steel with Near Random Crystallographic Orientation, *Annual Book of ASTM Standards*, ASTM, 2013.
- [29] V. Shrinivas, S.K. Varma, E. Murr, Deformation-induced martensitic characteristics in 304 and 316 stainless steels during room-temperature rolling, *Metall. Mater. Trans. A* 26 (1995) 661–671.
- [30] L. Murr, K. Staudhammer, S. Hecker, Effects of strain state and strain rate on deformation-induced transformation in 304 stainless steel: Part II. Microstructural study, *Metall. Trans. A* 13 (1982) 627–635.
- [31] H.W. Huang, Z.B. Wang, J. Lu, K. Lu, Fatigue behaviors of AISI 316L stainless steel with a gradient nanostructured surface layer, *Acta Mater.* 87 (2015) 150–160.
- [32] H.W. Zhang, Z.K. Hei, G. Liu, J. Lu, K. Lu, Formation of nanostructured surface layer on AISI 304 stainless steel by means of surface mechanical attrition treatment, *Acta Mater.* 51 (2003) 1871–1881.
- [33] N.R. Tao, X.L. Wu, M.L. Sui, J. Lu, K. Lu, Grain refinement at the nanoscale via mechanical twinning and dislocation interaction in a nickel-based alloy, *J. Mater. Res.* 19 (2004) 1623–1629.
- [34] X.H. Chen, J. Lu, L. Lu, K. Lu, Tensile properties of a nanocrystalline 316L austenitic stainless steel, *Scr. Mater.* 52 (2005) 1039–1044.
- [35] A. Weidner, S. Martin, V. Klemm, U. Martin, H. Biermann, Stacking faults in high-alloyed metastable austenitic cast steel observed by electron channelling contrast imaging, *Scr. Mater.* 64 (2011) 513–516.
- [36] X. Yang, S. Sun, T. Zhang, The mechanism of bcc α' nucleation in single hcp ϵ laths in the fcc γ -hcp $\epsilon \rightarrow$ bcc α' martensitic phase transformation, *Acta Mater.* 95 (2015) 264–273.
- [37] Y. Tian, O.I. Gorbatov, A. Borgenstam, A.V. Ruban, P. Hedström, Deformation microstructure and deformation-induced martensite in austenitic Fe-Cr-Ni alloys depending on stacking fault energy, *Metall. Mater. Trans. A* 48 (2017) 1–7.
- [38] N. Gey, B. Petit, M. Humbert, Electron backscattered diffraction study of ϵ/α' martensitic variants induced by plastic deformation in 304 stainless steel, *Metall. Mater. Trans. A* 36 (2005) 3291–3299.
- [39] N. Nakada, H. Ito, Y. Matsuoka, T. Tsuchiyama, S. Takaki, Deformation-induced martensitic transformation behavior in cold-rolled and cold-drawn type 316 stainless steels, *Acta Mater.* 58 (2010) 895–903.
- [40] J.A. Venables, The martensite transformation in stainless steel, *Philos. Mag.* 7 (1962) 35–44.
- [41] F. Lacroix, A. Pineau, Martensitic transformations induced by plastic deformation in the Fe-Ni-Cr-C system, *Metall. Trans.* 3 (1972) 391–400.
- [42] F.K. Yan, G.Z. Liu, N.R. Tao, K. Lu, Strength and ductility of 316L austenitic stainless steel strengthened by nano-scale twin bundles, *Acta Mater.* 60 (2012) 1059–1071.
- [43] C.S. Hong, N.R. Tao, X. Huang, K. Lu, Nucleation and thickening of shear bands in nano-scale twin/matrix lamellae of a Cu-Al alloy processed by dynamic plastic deformation, *Acta Mater.* 58 (2010) 3103–3116.
- [44] M. Calmunger, G. Chai, R. Eriksson, S. Johansson, J.J. Moverare, Characterization of austenitic stainless steels deformed at elevated temperature, *Metall. Mater. Trans. A* 48 (2017) 4525–4538.
- [45] J.W. Christian, S. Mahajan, Deformation twinning, *Prog. Mater. Sci.* 39 (1995) 4.

- [46] M.H. El-Axir, Int. J. Mach. An investigation into roller burnishing, *Tools Manuf.* 40 (11) 1603–1617.
- [47] M. Uddin, C. Hall, R. Hooper, E. Charrault, P. Murphy, V. Santos, Finite element analysis of surface integrity in deep ball-burnishing of a biodegradable AZ31B Mg alloy, *Metals* 8 (2018) 136.
- [48] M. Munawar Chaudhri, Strain hardening around spherical indentations, *Phys. Stat. Sol.* 182 (2000) 641–652.
- [49] P.K. Rai, V. Pandey, K. Chattopadhyay, L.K. Singhal, V. Singh, Effect of ultrasonic shot peening on microstructure and mechanical properties of high-nitrogen austenitic stainless steel, *J. Mater. Eng. Perform.* 23 (2014) 4055–4064.
- [50] G.S. Mahobia, C.S. Kumar, K. Chattopadhyay, Nanocrystallisation of nickel free high nitrogen austenitic stainless steel through ultrasonic shot peening, *Key Eng. Mater.* 813 (2019) 43–48.